

UNIVERSITÀ DI NAPOLI “FEDERICO II”



FLUIDODINAMICA NUMERICA

INGEGNERIA AEROSPAZIALE

Three-dimensional Driven Cavity flow

Author:

Andrea RUSSO

Supervisor:

Prof. G. COPPOLA



Academic Year 2024-2025

Abstract

This study explores a 3D lid-driven cavity simulation employing the UPV method, which ensures precise coupling between velocity and pressure fields in incompressible flows using a Harlow-Welch (staggered) grid. The primary objective is to identify the maximum Reynolds number at which the method remains both stable and accurate. Through comprehensive numerical analysis, the study defines the operational limits of the model before the onset of instabilities.

1 Introduction

The lid-driven cavity problem serves as a classical benchmark in fluid dynamics, widely used to assess numerical methods for incompressible flows. Early research by Freitas et al. [1] highlighted the complexities of simulating three-dimensional cavity flows, emphasizing the delicate balance between flow structures and numerical stability. Subsequent advancements, such as those by Albensoeder and Kuhlmann [2], provided a more refined understanding of these flows. Their approach utilized a Chebyshev collocation method for spatial discretization and an Adam-Bashforth scheme for time integration. By representing the solution as a superposition of stationary local asymptotic solutions and a residual flow field, they achieved a precise and accurate depiction of the flow behavior. This study, on the other hand, adopts the UVP method to examine the stability and accuracy of 3D lid-driven cavity simulations, with a focus on identifying the maximum attainable Reynolds number before numerical instabilities arise. The accuracy of the simulations will be evaluated by comparing the obtained results, whenever possible, with those reported in the literature.

2 Theoretical background

2.1 Three dimensional Navier-Stokes equations for Incompressible Viscous Fluids

The system that we intend to resolve comprises the three momentum conservation equations and the mass conservation one, which results in the following:

$$\begin{cases} \rho \left(\frac{\partial \mathbf{u}}{\partial t} + \nabla \cdot (\mathbf{u} \otimes \mathbf{u}) \right) = -\nabla p + \mu \nabla^2 \mathbf{u}, \\ \nabla \cdot \mathbf{u} = 0. \end{cases}$$

where:

- ρ is the fluid density,
- \mathbf{u} is the velocity field of the fluid,
- t is time,
- p is the pressure,
- μ is the dynamic viscosity of the fluid.

From these two we can then derive a secondary equation, the Pressure Poisson Equation (PPE):

$$(1) \quad \nabla^2 p = \rho \nabla \cdot \left(\frac{\partial \mathbf{u}}{\partial t} + \mathbf{u} \cdot \nabla \mathbf{u} \right),$$

A closer inspection of this equation clearly reveals the root of the problem: it is elliptic. This implies that pressure disturbances propagate instantaneously throughout the fluid, as expected due to the very low Mach number. Consequently, there is no evolution equation available for directly computing PP, nor can a time-marching approach be applied. In the past, (name) attempted to introduce a fictitious time evolution for the pressure, but this method has since been significantly outperformed by more advanced techniques.

2.2 UVP Method

This method circumvents the absence of a pressure evolution equation by initially computing an intermediate velocity field \mathbf{V}^* without accounting for the pressure contribution, thus not satisfying the continuity equation. Subsequently, a "pressure correction" is determined based on this intermediate field to ensure that the final velocity field is divergence-free. Let's explore this procedure in more detail.

The first step involves calculating \mathbf{V}^* , the velocity field update obtained by excluding the pressure gradient:

$$(2) \quad \frac{d\mathbf{V}^*}{dt} = \mathbf{R}(\mathbf{V}) \quad \text{con} \quad \mathbf{R}(\mathbf{V}) = \nabla \cdot (\mathbf{V}\mathbf{V}) + \nu \nabla^2 \mathbf{V}$$

Now, if we consider the real update of the field that we want to obtain, \mathbf{V}_{n+1} , it is clear that \mathbf{V}^* shares its curl with \mathbf{V}_{n+1} :

$$\frac{d\mathbf{V}_{n+1}}{dt} = \mathbf{R}(\mathbf{V}) + \nabla P$$

$$\nabla \times \mathbf{V}^* = \nabla \times \mathbf{V}_{n+1}$$

That's because the difference between the two is a gradient, which is obviously irrotational.

The next step involves obtaining the so-called "pressure correction." To derive the correct velocity field starting from \mathbf{V}^* , we must modify it without altering its curl. This implies adding a component that is irrotational and can thus be expressed as the gradient of a scalar field:

$$\mathbf{V}_{n+1} = \mathbf{V}^* + \nabla \phi$$

How do we obtain ϕ ? It is important to note that we cannot simply add any gradient: the correction must be applied in such a way that the resulting velocity field is divergence-free, so:

$$(3) \quad \nabla \cdot \mathbf{V}^* = -\nabla^2 \phi$$

and that's how we get our condition on ϕ .

Let's now take a quick look at Eq. (1) and Eq. (2). From these, it can be derived that:

$$(4) \quad \nabla \cdot \mathbf{V}^* = (\nabla^2 P) \Delta t$$

By merging Eq. (3) and Eq. 4, we can see that the scalar potential ϕ is actually P_{n+1} :

$$\nabla^2 P \Delta t = -\nabla^2 \phi$$

So, the velocity field for $t = t_{n+1}$ will be:

$$\mathbf{V}_{n+1} = \mathbf{V}^* - \nabla P_{n+1} \Delta t$$

2.3 Helmholtz-Hodge decomposition theorem

Further proof that the procedure described is indeed correct can be found by considering the Helmholtz-Hodge decomposition theorem. This theorem states that any sufficiently regular field \mathbf{V} can be decomposed as:

$$\mathbf{V} = -\nabla \phi + \nabla \times \mathbf{A}$$

where $\nabla \times \mathbf{A}$, by definition, is a field that shares the curl with our field \mathbf{V} . Therefore, it corresponds to \mathbf{V}^* .

The theorem further states that, for this decomposition to be computed, it is also necessary to know the values of:

1. $\nabla \times \mathbf{V} = P$
2. $\nabla \cdot \mathbf{V} = s$
3. $\mathbf{V} \cdot \hat{\mathbf{n}} = f$

In our case, it is known that the divergence is actually 0. Now, we can impose that the divergence of \mathbf{V} is given by s :

$$\nabla \cdot \mathbf{V} = s = \nabla \cdot \mathbf{P} + \nabla^2 \phi$$

Naturally, solving the Poisson problem also requires boundary conditions, which can be obtained by projecting Eq. (2) along $\hat{\mathbf{n}}$:

$$\frac{\partial \phi}{\partial \hat{\mathbf{n}}} = \mathbf{V} \cdot \hat{\mathbf{n}} - \mathbf{P} \cdot \hat{\mathbf{n}}$$

One could now argue that, since we are using homogeneous Neumann boundary conditions, ϕ will be defined up to a constant. However, this does not pose a problem, as the quantity needed to represent \mathbf{V} is the gradient of ϕ , which will naturally eliminate the constant.

Thus, what we have just demonstrated is that our UVP procedure is essentially a Helmholtz-Hodge decomposition, where \mathbf{P} corresponds to \mathbf{V}^* , and ϕ is ∇P_{n+1} .

2.4 Harlow-Welch discretization

2.4.1 Why is it needed?

A Harlow-Welch grid (or staggered grid) is a mesh in which not all variables are collocated at the same location. Specifically, if we denote the spatial step as h , the grid for the u field is shifted by $h/2$ along the x -axis, and the grid for the v field is shifted by $h/2$ along the y -axis. In two dimensions, this results in a mesh structured as follows:

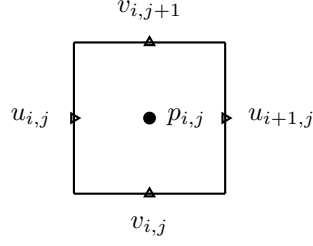
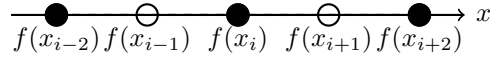


Figure 1: Harlow-Welch staggering in 2D

Now, why is this type of mesh necessary? It stems from the fact that using a collocated mesh combined with central stencils for the first-order derivatives results in a wide stencil for the second-order derivative, specifically $[1 \ 0 \ -2 \ 0 \ 1]$, and consequently for the Laplacian as well.



This, in turn, will lead to two decoupled pressure fields: one defined on the odd indexes and the other on the even indexes. This situation is clearly unphysical and will result in spurious currents and, eventually, numerical instabilities.

By adopting a staggered mesh, we can still apply a central scheme, but now on a stencil of size h instead of $2h$. This allows us to regain a compact stencil for the second-order derivative and effectively avoid spurious currents.

2.4.2 How will it be implemented in 3D?

In three dimensions, we will still shift the u and v fields by $h/2$ along the x and y axes, respectively, but we will also shift the field by $h/2$ along the z -axis.

This results in the following configuration:

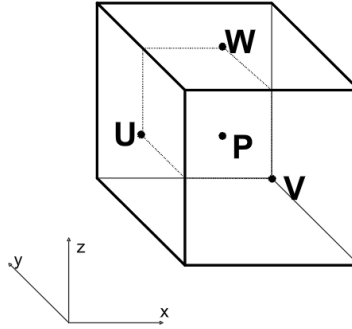


Figure 2: Placements on the mesh of the interpolated variables in the center.

Since we are now employing a central scheme with a spatial step of h , we must adjust the calculation of the derivatives in the convective term accordingly. Specifically, we need to determine how to compute:

$$\begin{array}{ccc} \frac{\partial u u}{\partial x} & \frac{\partial v v}{\partial y} & \frac{\partial w w}{\partial z} \\ \frac{\partial u v}{\partial y} & \frac{\partial u w}{\partial z} & \frac{\partial v u}{\partial x} \end{array}$$

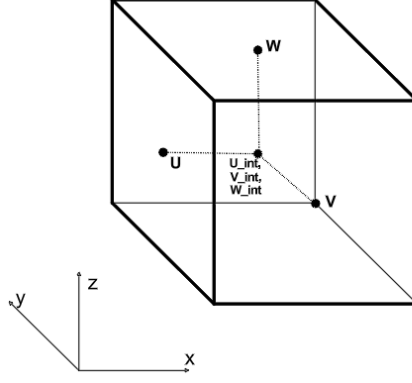


Figure 3: Placements on the mesh of the interpolated variables in the center.

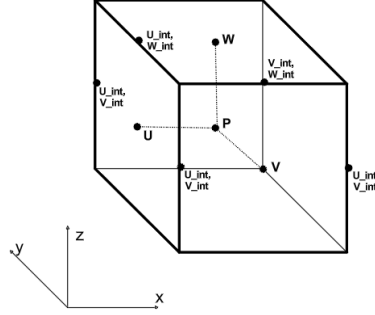


Figure 4: Placements on the mesh of the interpolated variables on the center of the edges.

$$\frac{\partial vw}{\partial z} \quad \frac{\partial wu}{\partial x} \quad \frac{\partial wv}{\partial y}$$

We will derive said expressions by first performing an interpolation at the center of the control volumes and then applying the respective derivatives, as shown in fig. 3.

Then, we will interpolate u, v and w on the center of our cube's edges, as shown in fig. 4. We will then calculate u^*v , v^*w , u^*w , and now, we'll be able to obtain the desired derivatives. This process can be represented with a single formula:

$$\delta^- \left(\frac{\bar{u}_i^{j+} \bar{u}_j^{i+}}{\delta x_j} \right)$$

$$where \quad \bar{u}^j = \frac{u_{i,j+1} + u_{i,j}}{2} \quad and \quad \delta^- = u_{i,j} - u_{i-1,j}$$

with i, j varying on x, y and z .

3 Results

The simulation was tested for Reynolds numbers equal to 100, 400, and 1000; this choice was not arbitrary, but was intended to best replicate the conditions in [1] and [2]. As we will see, the higher the Reynolds number, the more our results will differ from those in the papers. In particular, the local maxima and minima observed will be less sharp, which

is a clear indication that we are over-diffusing. Furthermore, the method implemented in both papers is of a higher order, so some differences are to be expected.

First off, to give an idea of the field in figure 5,6,7 the field is represented in 3D using streamlines in the $z = 0.1, 0.5, 0.9$ planes. It seems clear by looking at the figures the birth of the same kind of structures at all Reynolds. The primary vortex takes place in the center of the field, as expected. What's evidently missing are the secondary vortices, possibly because of the lower order of our method (2nd against 4th) and the lower resolution used (32x32x32 was already a lot to handle for my CPU).

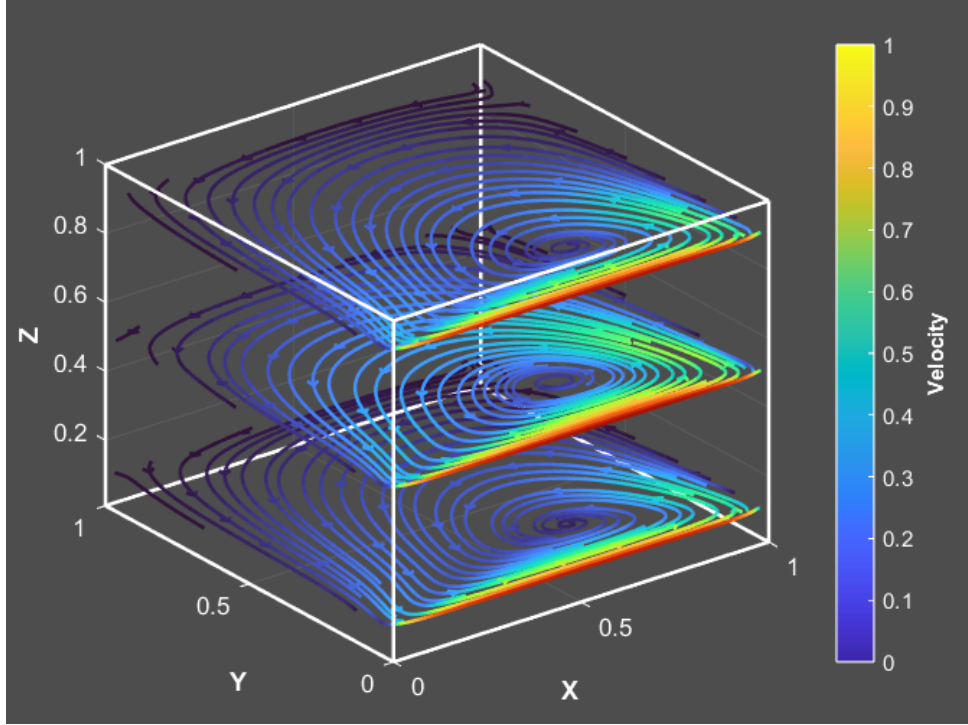


Figure 5: Streamlines in the $z = 0.1, 0.5, 0.9$ planes for $Re = 100$.

Now, instabilities begin to appear when the Reynolds number exceeds 1000, regardless of how much we reduce the Courant number. It is important to note that the Courant number is already particularly low in the results presented here: it is set to 0.1 for both $Re = 100$ and $Re = 400$. However, for $Re = 1000$, the Courant number had to be further reduced to $C = 0.05$ in order to prevent the onset of instabilities. This adjustment was crucial in maintaining the stability of the simulation. The data presented in the following figures has been meticulously extracted from the work of [1], specifically for the case where the cavity is cubic, meaning that all sides have the same length. So, the higher the Reynolds, the more the results become inaccurate. In particular, as already said, they seem to be over-diffused. This clearly shows that the truncation error is of an anti-diffusive type, and not considering it would result in higher values. As for the grid dimensions, a 32x32x32 grid has been used, to be faithful to the paper's results. Everything is presented in Figure 8.

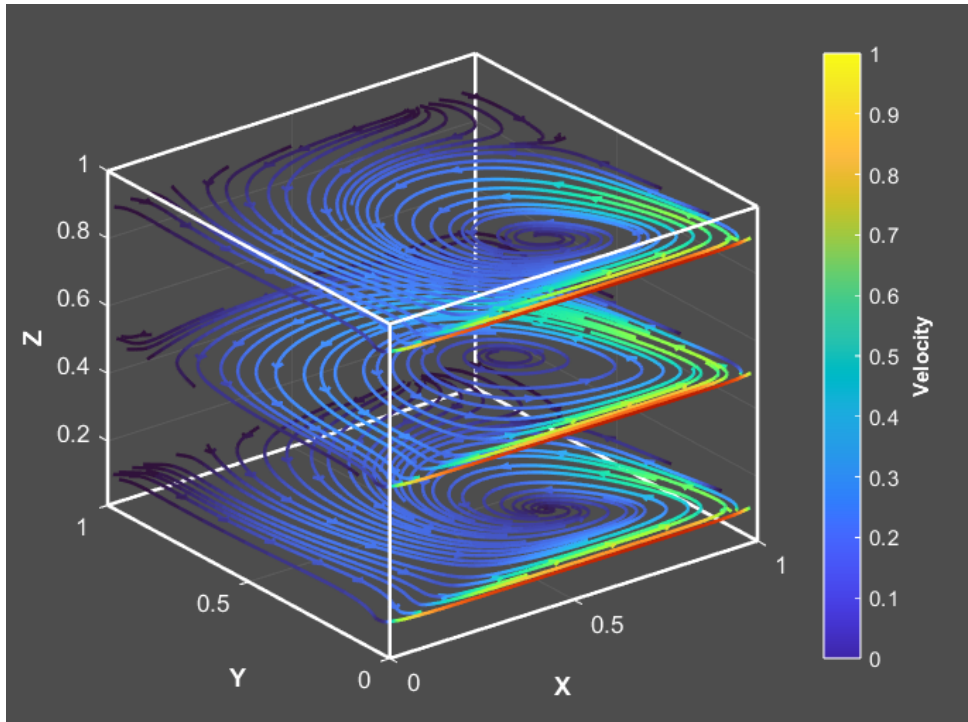


Figure 6: Streamlines in the $z = 0.1, 0.5, 0.9$ planes for $Re = 400$.

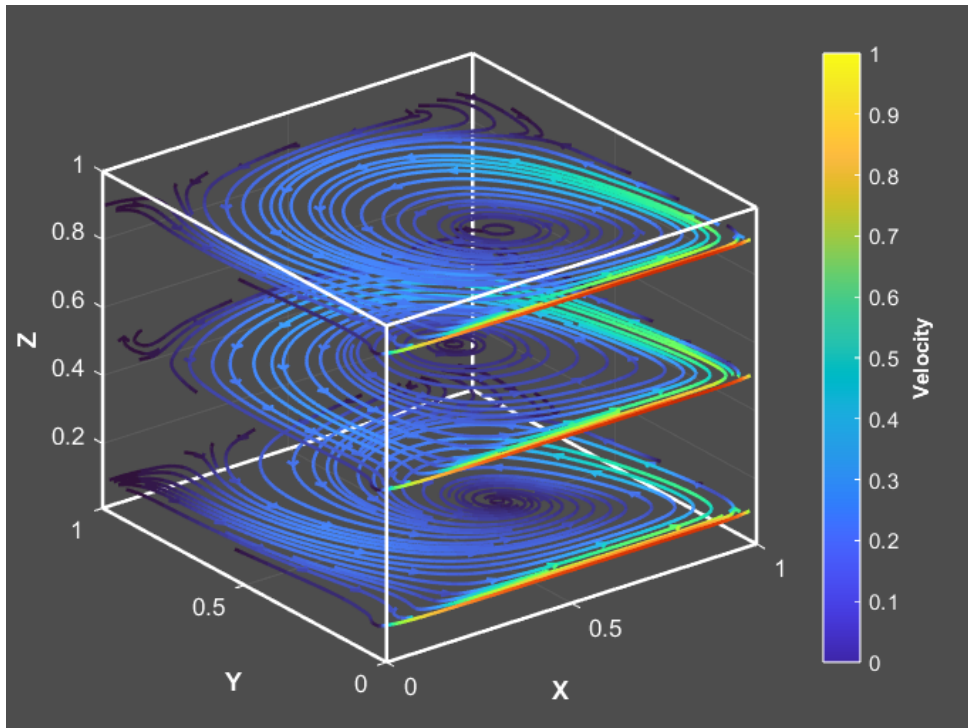


Figure 7: Streamlines in the $z = 0.1, 0.5, 0.9$ planes for $Re = 1000$.

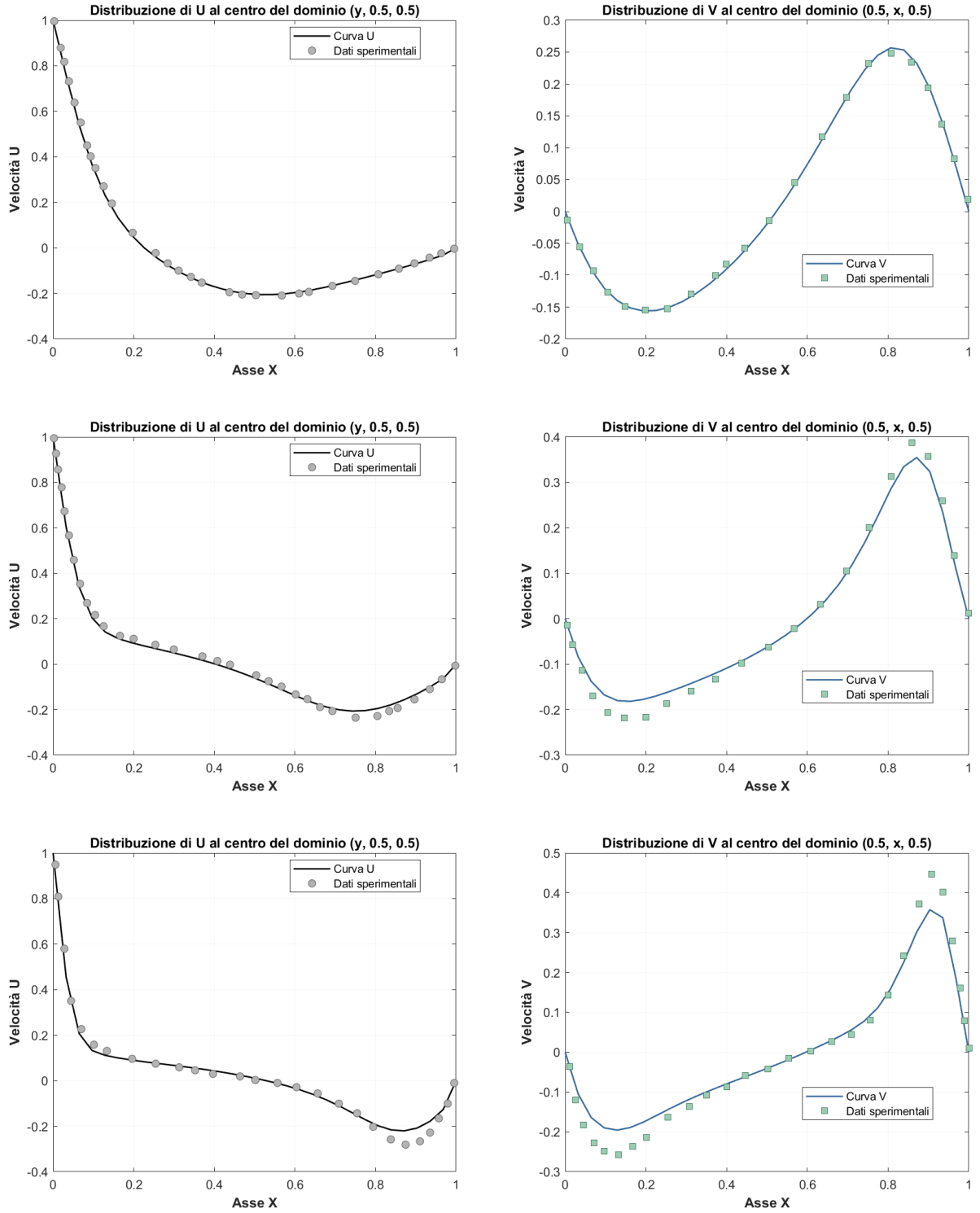


Figure 8: Velocity distribution of U and V along the centerline of the domain at different Reynolds numbers ($Re = 100, 400, 1000$). The images on the left show the distribution of U at $(y, 0.5, 0.5)$, while the images on the right represent the distribution of V at $(0.5, x, 0.5)$. The increase in Re highlights the evolution of the velocity profiles.

3.1 Comparison with results from Hwar et al.

As further confirmation of the reliability of our results, we present here the results of [2], which, although using a different method, they clearly obtain the birth of the same kind of flow structures. This paper uses a Chebyshev pseudospectral technique.

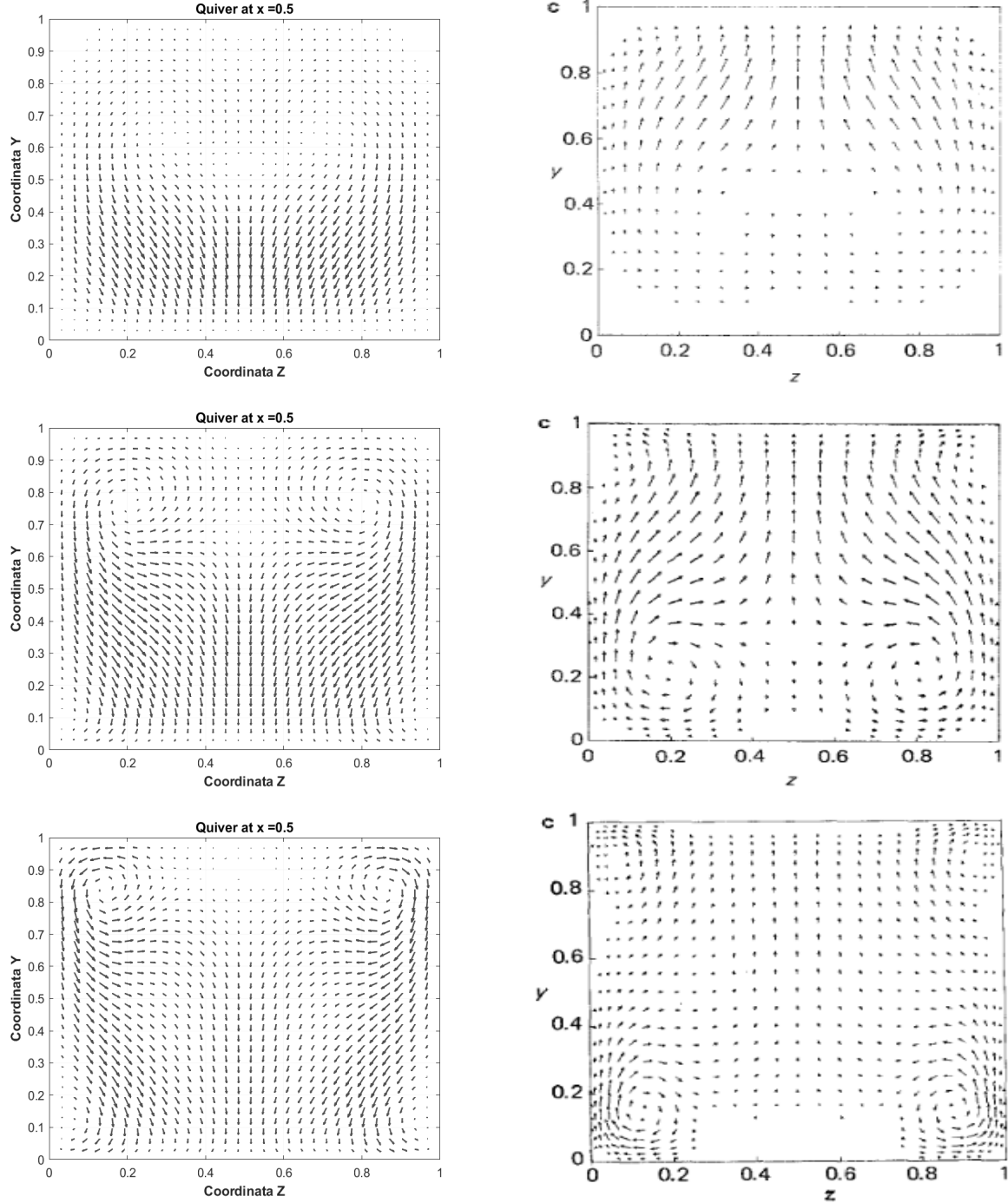


Figure 9: Comparison between the quiver plots of our results (left column) and those of Ghia et al. (right column) at different Reynolds numbers ($Re = 100, 400, 1000$). The figures represent the vector field at $x = 0.5$, highlighting the similarities between the simulations.

References

- [1] S. Albensoeder , H.C. Kuhlmann *Accurate three-dimensional lid-driven cavity flow.* Journal of Computational Physics **206**, (2005) 536–558
- [2] Hwar C. Ku, Richards S. Hirsh, and Thomas D. Taylor *A pseudospectral method for solution of the Three-Dimensional Incompressible Navier-Stokes Equations.* Journal of Computational Physics **70**, (1987) 439-462